Journal Pre-proof

Low-cycle fatigue life prediction of a polycrystalline nickel-base superalloy using crystal plasticity modelling approach

Guang-Jian Yuan, Xian-Cheng Zhang, Bo Chen, Shan-Tung Tu, Cheng-Cheng Zhang

Please cite this article as: Yuan G-Jian, Zhang X-Cheng, Chen B, Tu S-Tung, Zhang C-Cheng, Low-cycle fatigue life prediction of a polycrystalline nickel-base superalloy using crystal plasticity modelling approach, *Journal of Materials Science and amp; Technology* (2019), doi: https://doi.org/10.1016/j.jmst.2019.05.072

Research Article

Low-cycle fatigue life prediction of a polycrystalline nickel-base superalloy using crystal plasticity modelling approach

Guang-Jian Yuan [a], Xian-Cheng Zhang [a,*], Bo Chen [b], Shan-Tung Tu [a,*], Cheng-Cheng Zhang [c]

[a] *Key Laboratory of Pressure Systems and Safety, Ministry of Education, School of Mechanical and Power Engineering, East China University of Science and Technology, Shanghai 200237, China*

[b] *The Institute for Advanced Manufacturing and Engineering, Faculty of Engineering, Environment and Computing, Coventry University, Coventry CV65LZ, UK*

[c] *AECC Commercial Aircraft Engine Co. LTD, Shanghai Engineering Research Center for Commercial Aircraft Engine, Shanghai 201108, China*

* Corresponding authors: *E-mail addresses:* xczhang@ecust.edu.cn (X.C. Zhang); sttu@ecust.edu.cn (S.T. Tu).

Abstract

A crystal plasticity model is developed to predict the cyclic plasticity during the low-cycle fatigue of GH4169 superalloy. Accumulated plastic slip and energy

dissipation as fatigue indicator parameters (FIPs) are used to predict fatigue crack initiation and the fatigue life until failure. Results show that fatigue damage is most likely to initiate at triple points and grain boundaries where severe plastic slip and energy dissipation are present. The predicted fatigue life until failure is within the scatter band of factor 2 when compared with experimental data for the total strain amplitudes ranging from 0.8% to 2.4%. Microscopically, the adjacent grain arrangements and their interactions account for the stress concentration. In addition, different sets of grain orientations with the same total grain numbers of 150 were generated using the present model. Results show that different sets have significant influence on the distribution of stresses between each individual grain at the meso-scale, although little effect is found on the macroscopic length-scale.

Keywords: Crystal plasticity; Fatigue; Finite element; Life prediction; Micro-mechanics; Nickel-base superalloy

1. Introduction

Nickel-base GH4169 superalloy exhibits relatively high strength, oxidation resistance, good formability and weldability due to its microstructural stability under thermo-mechanical loads[1,2]. The components manufactured by nickel-base superalloys, such as turbine discs in aero-engines, are often subjected to cyclic loads that cause the low-cycle fatigue (LCF) failure[3]. Therefore, it is important to develop a mechanistic understanding on the LCF deformation and damage process in nickel-base superalloy. Chen et al.[4] investigated the effect of strain amplitude on LCF life of GH4169. It was found that fatigue lives decreased significantly with increasing total strain amplitude. In addition, a fatigue life prediction model based on the fatigue damage parameter was developed by Wei et al.[5] for LCF in GH4169 superalloy. The model predicted LCF lives for a range of total strain amplitudes were found to be within the scatter band of factor 2 when compared to the LCF test data. The above-

mentioned studies focused on the macro-scopic LCF behaviour of GH4169 superalloy. However, limited work has been undertaken on the meso-scale modelling of this superalloy. To this end, the present work is aimed to provide a mechanistic understanding on the cyclic deformation behaviour and associated damage accumulation, by establishing a crystal plasticity type modelling framework and then implementing the model to study the LCF crack initiation and life prediction.

The crystal plasticity finite element method (CPFEM) was first proposed by Pierce et al.[6] to investigate the tensile behaviour of a single crystal. Due to the heavy computational cost, only two symmetric slip systems were considered in their model. Later, the CPFEM was extended to a polycrystalline material by Harren et al.[7] using a 2D model to study mechanical responses of a polycrystalline copper under the tensile, compressive and shearing loads. Becker[8] then performed simulation of channel die compression on the basis of 12 slip systems in a face-centred-cubic aluminium polycrystalline material. An ever-increasing number of work[9-11] based on the CPFEM has been performed because of the increased computational power. Dunne and Manonukul[12] pioneered the CPFEM work to study the crack initiation behaviour in both the LCF and high-cycle fatigue (HCF) of a nickel-base superalloy. In addition, Guan et al.[13] further studied the strain localisation behaviour under fatigue of both single crystal and directionally solidified nickel-base superalloys by using both the CPFEM and high-resolution digital image correlation technique. Most of the recent crystal plasticity type work on nickel-base superalloys[14-16] that included a large number of material parameters (up to 13) can provide a very accurate prediction of the material behaviour. However, such CPFEM models come with the high degree of complexity that might not be practical for engineering applications.

Furthermore, one of the key parameters used in the CPFEM models to determine the damage accumulation and associated fatigue life until failure is the so-called fatigue indicator parameter (FIP). For example, Dunne and Manonukul[12] used accumulated plastic slip to predict fatigue crack initiation in nickel-base superalloy C263 under both HCF and LCF conditions successfully. The work undertaken by

Dunne et al.[17] showed that the fatigue crack initiation position and crack growth behaviour were in good agreement with experimental observations. It is also worth noting that some researchers[18-20] suggested that dissipated energy could be used as an FIP to determine the damage accumulation. To this end, the present paper compares the accumulated plastic slip, p_{crit}, and dissipated energy, W_{crit}, in terms of predicting the LCF crack initiation and fatigue life until failure. The GH4169 superalloy and the LCF testing are described in the next section, followed by the presentation of the CPFEM model development and its application to study both the macroscopic and meso-scale fatigue behaviour as well as LCF life prediction.

2. Materials and mechanical testing

The precipitation-strengthened GH4169 nickel-base superalloy was provided by Fushun Special Steel Shares Co., Ltd, China. Additional heat treatments were given to the as-supplied material: solution annealing and thermal aging. The solution annealing was performed at 960 °C for 1 h and then cooling to room temperature in air. The thermal aging was first conducted at 720 °C for 8 h, followed by a controlled cooling to 620 °C with a cooling rate of 50 °C/h. The second step thermal aging was performed at 620 °C for 8 h and then air cooling to room temperature. The chemical composition of the GH4169 superalloy is given in Table 1.

Samples for microstructural examination were prepared following standard metallographic procedures[21]. A Zeiss Evo® MA 15 scanning electron microscope (SEM) was used for microstructural observation. Fig. 1 shows a typical microstructure of GH4169, obtained by SEM. The average grain size of the material was measured to be 14±1 μm. The presence of intergranular δ phase precipitates can be seen in Fig. 1. Electron backscattered (EBSD) orientation maps were obtained with the HKL Channel 5 software, using an FEI Quanta 3D FEG-SEM (20kV for beam current) with a step size of 1 μm. The EBSD orientation map and pole figure in Fig. 2(a) and (b) show that the GH4169 superalloy has a typical texture-free microstructure.

A tensile test was undertaken on a cylindrical bar type specimen with the gauge dimension of 5 mm in diameter and 25 mm in length. The tensile test was performed with a constant loading rate of 0.01 mm/s. An extensometer attached onto the specimen gauge area was used to measure the mechanical strain during the tensile deformation. The stress−strain behaviour during the tensile loading of GH4169 superalloy was used to calibrate the model input parameters. More details about the model calibration will be given in Section 5.1.

Fully reversed strain-controlled LCF tests were carried out at a constant strain rate of 8×10^{-3} s^{-1}. The following total strain amplitudes $\Delta \varepsilon_t$ were selected: 2.4%, 2.0%, 1.6%, 1.2%, 1.0% and 0.8%. The dimension of LCF test specimens within the gauge section is 5.5 mm in diameter and 12 mm in length. Furthermore, in order to control the roughness of the machined surface of specimen, the surface was mechanical polished up to a mirror finish (Ra=0.8).

Like the tensile test, the macro-scopic strain was monitored by the attached extensometer and used to perform the strain-controlled LCF tests. Total material separation was regarded as the failure of specimen (i.e. the end of the fatigue test)[22]. These LCF test data were used to compare with the crystal plasticity based model outputs in terms of both the cyclic stress−strain behaviour as well as the fatigue life until failure.

3. Crystal plasticity framework and numerical implementation

3.1 Crystal plasticity theory

When a load is applied to a polycrystalline material, the total deformation and rotation of each individual crystal can be described by deformation gradient F:

$$F = F_e \cdot F_p \qquad (1)$$

where F_e denotes deformation gradient caused by stretching and rotation of the crystal lattice, and F_p denotes plastic deformation of the crystal lattice along slip

direction.

For the plastic deformation due to slip, the plastic velocity gradient L_p can be related to the plastic slip rate $\dot{\gamma}_\alpha$ on the αth slip system by the following[23]:

$$L_p = \dot{F}_p \cdot F_p^{-1} = \sum_\alpha \dot{\gamma}_\alpha s_\alpha \otimes m_\alpha \tag{2}$$

where s_α and m_α are slip direction vector and slip normal plane vector on the αth slip system, respectively.

According to Schmid's law, the slip system will be activated when the magnitude of the resolved shear stress τ_α is greater than the critical value (i.e. critical resolved shear stress). The resolved shear stress τ_α on the αth slip system can be defined as:

$$\tau_\alpha = (m_\alpha \otimes s_\alpha) : \sigma \tag{3}$$

The relation between resolved shear stress τ_α and plastic slip rate $\dot{\gamma}_\alpha$ on the αth slip system can be described by the classic viscoplastic flow rule[7]:

$$\dot{\gamma}_\alpha = \dot{\gamma}_0 \, \mathrm{sgn}(\tau_\alpha - \chi_\alpha) \left\{ \left| \frac{\tau_\alpha - \chi_\alpha}{g_\alpha} \right| \right\}^n \tag{4}$$

where $\dot{\gamma}_0$ is the reference strain rate and n represents the rate sensitivity exponent related to material properties. Parameter n is the power law exponent that represents strain-rate sensitivity. The rate-independent limit can be obtained when n tends to be ∞[24]. Here, a fixed value of $n=100$ was used for the rate-dependent crystal plasticity model. The term $\dot{\gamma}_0$ denotes the reference plastic slip rate; a value of 0.001 was used for all slip systems. χ_α is the so-called back stress. Parameter g_α is the current strength variable on the αth slip system, which is defined by:

$$\dot{g}_\alpha = \sum_\beta h_{\alpha\beta} \dot{\gamma}_\beta \tag{5}$$

where $\dot{\gamma}_\beta$ is the plastic slip rate on the βth slip system, $h_{\alpha\beta}$ is the slip hardening matrix, or the so-called latent hardening moduli that can be defined as:

$$h_{\alpha\beta} = qh_{\alpha\alpha} = h_0 \operatorname{sech}^2 \left| \frac{h_0 \gamma_\alpha}{g_\infty - \tau_0} \right| \qquad (6)$$

where q sets the level of latent hardening moduli $h_{\alpha\beta}$ as compared to the self-hardening moduli $h_{\alpha\alpha}$. The most commonly used q value ranges between 1 and 1.4[25]. Here the q value was taken as 1 for simplicity. Parameters h_0, τ_0 and g_∞ are the initial hardening modulus, critical resolved shear stress and saturation stress, respectively. They are all material constants. γ_α is the accumulated plastic slip on the αth slip system, which is the integral of the plastic slip rate $\dot{\gamma}_\alpha$ over the time interval:

$$\gamma_\alpha = \sum_\alpha \int_0^t |\dot{\gamma}_\alpha| dt \qquad (7)$$

The back stress χ_α in Eq. (4) that accounts for the kinematic hardening follows the nonlinear evolution rule[26]:

$$\dot{\chi}_\alpha = C\dot{\gamma}_\alpha - D\chi_\alpha |\dot{\gamma}_\alpha| \qquad (8)$$

where C and D are the initial hardening modulus and the rate of decline corresponding to how the material responses upon loading.

Two types of FIPs were used in the present model as the LCF failure criteria to determine the fatigue crack initiation dominated failure life; they are accumulated plastic slip and energy dissipation. The plastic slip p has been previously proved to be effective for predicting both the LCF and HCF lives in nickel-base superalloy C263[12]. In detail, the plastic slip p can be defined as:

$$\dot{p} = (\frac{2}{3} L_p : L_p)^{1/2} \qquad (9)$$

$$p = \int_0^t \dot{p} dt \qquad (10)$$

In addition, the strain energy dissipation W[19] can be written as:

$$W = \sum_\alpha \int_0^t \tau_\alpha \dot{\gamma}_\alpha dt \qquad (11)$$

The critical value of the accumulated plastic slip p_{crit} is related to the cycles of fatigue to crack initiation. It is important to note that this parameter is often obtained

through fitting to experimental data. In another word, the value of p_{crit} equates to the

product between the experimentally obtained cycles to fatigue crack initiation N_i and

the modelling predicted plastic slip per cycle p_{cyc} as given below:

$$p_{crit} = N_i \cdot p_{cyc} \qquad (12)$$

Similarly, the critical accumulated energy dissipation W_{crit} can be determined

by:

$$W_{crit} = N_i \cdot W_{cyc} \qquad (13)$$

Here two types of FIPs (accumulated plastic slip and energy dissipation) were

used to investigate the life prediction ability. The fatigue indicator parameters have

been widely used to predict the fatigue initiation life[27,28]. The aim of this work is to

compare the life prediction ability between plastic slip p and strain energy dissipation

W for GH4169 superalloy.

Where applicable, the number of cycles to 5% drop in the stabilized load range

was assumed as the fatigue initiation life in nickel-based superalloy Inconel 718[29]

which means that the fatigue crack initiation life N_i is approximately equal the fatigue

failure life (i.e. $N_i \approx N_f$), as previously discussed[12]. This should apply to both the

plastic slip and energy dissipation based fatigue failure criteria. In summary, the

present crystal plasticity model requires seven plasticity parameters: the reference

strain rate $\dot{\gamma}_0$, and the rate sensitivity exponent n in Eq. (3), the initial hardening

modulus h_0, the critical resolved shear stress τ_0 and the saturation stress g_∞ in Eq.

(6), the initial hardening modulus C and the rate of decline D in Eq. (8). Parameters n

and $\dot{\gamma}_0$ were set as constant without iteration. Other parameters h_0, τ_0, g_∞, C and D

in Eq. (6) and Eq. (8) were determined by trial-and-error method[30] by comparing to

uniaxial tensile data. In addition, three elastic constants (C_{11}, C_{12} and C_{44}) were also

derived from the best fitting to the macroscopic stress-strain curve (i.e. elastic

modulus E=198GPa and Poisson ratio v=0.3) in the elastic region of the uniaxial

tensile test. All the parameters of crystal plasticity model are listed in Table 2. It is a useful method to determine the material parameters based on the macro experiments[31,32]. Then the same material parameters were used to predict the stress-strain response under different conditions.

3.2 Numerical implementation

The above-mentioned crystal plasticity model was numerically implemented into UMAT by using time integration method to calculate plastic slip increment $\Delta\gamma_\alpha$ on the slip system:

$$\Delta\gamma_\alpha = (1-\theta)\Delta t\,\dot\gamma_{\alpha_t} + \theta\Delta t\,\dot\gamma_{\alpha_{t+\Delta t}} \tag{14}$$

where the subscripts t and $t+\Delta t$ represent the time when plastic slip rate $\dot\gamma_\alpha$ is calculated. The parameter θ is a constant that influences the numerical oscillations with its value ranging from 0 to 1[24]. For values of θ ranging from 0.5 to 1.0, the solutions are stable and accurate even up to large increment[33]. Therefore, a choice of θ between 0.5 to 1.0 is recommended. Here a value of $\theta=0.5$ was used.

The plastic slip rate $\dot\gamma_\alpha$ is a function related to the resolved shear stress τ_α and the current strength variable g_α, as defined in Eq. (4). The Taylor expansion of the plastic slip rate $\dot\gamma_\alpha$ is given by:

$$\dot\gamma_{\alpha_{t+\Delta t}} = \dot\gamma_{\alpha_t} + \frac{\partial\dot\gamma_\alpha}{\partial\tau_\alpha}\Delta\tau_\alpha + \frac{\partial\dot\gamma_\alpha}{\partial g_\alpha}\Delta g_\alpha \tag{15}$$

where $\Delta\tau_\alpha$ and Δg_α represent the increments of resolved shear stress and current strength during the time increment Δt on the αth slip system, respectively. The following relation can be obtained by combining Eqs. (14) and (15):

$$\Delta\gamma_\alpha = \Delta t\left[\dot\gamma_{\alpha_t} + \theta\frac{\partial\dot\gamma_\alpha}{\partial\tau_\alpha}\Delta\tau_\alpha + \theta\frac{\partial\dot\gamma_\alpha}{\partial g_\alpha}\Delta g_\alpha\right] \tag{16}$$

The plastic slip rate $\dot\gamma_\alpha$ within time increment, Eq. (15), is related to the plastic slip increment. To solve the iterative problem of plastic slip increment, the Newton-

Raphson method[34] was employed to achieve implicit solution. A larger time increment was allowed for the nonlinear solution procedure since the incremental relations were found to be more stable. Stress and strain state variables were evaluated at the end of the time increment ($t+\Delta t$).

The consistent tangent (consistent Jacabian) $\mathbb{C}$ can be defined as a rate-form constitutive law:

$$\mathbb{C}=\frac{1}{J}\frac{\partial\Delta\boldsymbol{\tau}}{\partial\Delta\boldsymbol{\varepsilon}} \tag{17}$$

where $\Delta\boldsymbol{\varepsilon}$ is the strain increment, $\boldsymbol{\tau}=J\boldsymbol{\sigma}$ is defined as the Kirchhoff stress and $\Delta\boldsymbol{\tau}$ is the Kirchhoff stress increment. In the crystal plasticity model, the definition of the consistent Jacobian relies on the definition of Kirchhoff stress increment as a function of strain increment. Here the Kirchhoff stress increment is written as:

$$\Delta\boldsymbol{\tau}=\overset{\triangledown}{\boldsymbol{\tau}}\Delta t \tag{18}$$

where $\overset{\triangledown}{\boldsymbol{\tau}}$ is the Jaumann rate of Kirchhoff stress that can be defined as:

$$\overset{\triangledown}{\boldsymbol{\tau}}=\dot{\boldsymbol{\tau}}\text{-}\boldsymbol{\Omega}\boldsymbol{\tau}+\boldsymbol{\tau}\boldsymbol{\Omega} \tag{19}$$

where $\boldsymbol{\Omega}$ is the sin rate related to the velocity gradient $\mathbf{L}$:

$$\boldsymbol{\Omega}=\frac{1}{2}\left(\mathbf{L}-\mathbf{L}_{\mathrm{T}}\right) \tag{20}$$

4. Crystal plasticity finite element modelling of GH4169

The polycrystalline aggregate was established by Voronoi tessellation (VT)[35]. This produced a representative volume element (RVE) for the GH4169 superalloy. The effect of the intergranular precipitation on the local stresses and strains at the meso-scale was not considered in the present work. A plane-train RVE type microstructure consisting of 150 grains was created for the crystal plasticity model, as illustrated in Fig. 3. Each grain of 12 slip systems with a face-centered cubic (FCC) structure was assigned randomly (i.e. texture-free) with an individual in-plane grain orientation.

The plastic deformation of the polycrystalline aggregate was calculated and analysed by the 2D crystal plasticity model mentioned in section 3. In this way, the relationships of stresses and strains in both the macroscopic and meso-scale were studied in detail. In addition, the inhomogeneous plastic strain field together with location-specific damage development was investigated.

The constraints and the coordinates of the crystal plasticity model are also illustrated in Fig. 3. All the nodes on the right side of the RVE were subjected to the same displacement in x direction upon loading while they were allowed to move freely in y direction. Meanwhile, all the nodes on the left side were constrained in x direction, while they could freely move in y direction. In addition, Since the RVE is generated based on the microstructure level that is small enough, multi-point constraints, shown in Fig. 3, were given to all the nodes on the top and bottom surfaces so that they had the same displacement in y direction. These constraints were applied to both the uniaxial tensile and fatigue CPFEM model predictions. This method is consistent with that reported by Sun et al.[36]. In terms of the macroscopic stress derivation, the engineering stress was calculated by dividing the applied force to the RVE with the initial area in the y direction (i.e. the initial width in Fig. 3). Similarly, the engineering strain can be obtained by dividing the displacement of RVE with the initial length in Fig. 3 in the x direction. Both the engineering stress and engineering strain were used in this work when calculating the macroscopic stresses and strains.

5. Results and discussion

5.1 Monotonic tensile behaviour

Fig. 4 shows a comparison of model simulated by using the fitted parameters and experimentally observed macroscopic stress–strain behaviour during the tensile loading of GH4169 superalloy. There was a good agreement between the model simulation and experimental data. This indicates that both the elasticity and plasticity

parameters selected in the present model could provide a reasonably good prediction to the monotonic mechanical response of the GH4169 superalloy. It is important to note that the crystal plasticity model with these calibrated parameters with respect to the monotonic tensile stress–strain curve were then used to predict the cyclic stress–strain deformation and meso-scale grain response in GH4169 superalloy.

Fig. 5 shows the distribution of the accumulated plastic slip during monotonic tensile loading, at the total engineering strains of 3.5%, 7% and 13%, respectively. The presence of localised, intergranular type plastic slip can be observed in Fig. 5(b) when the material was strained to 7%. The level of the localised plastic slip increased with the increasing strain to 13%. Most of the slip bands within the grains or close to the grain boundaries were observed to have approx. 45° angles relative to the loading direction (i.e. the horizontal direction). Two groups of grains are indicated in Fig. 5(c). It can be seen that grains 1, 2 and 3 (belong to group 1) have a more intensive localised plastic slip. The slip system angles to the loading direction of grains 1 to 3 were found to be 68.61°, 72.63° and 50.93°, respectively. When compared to the slip system angles of grains 4 to 6 (belong to group 2), that had 80.60°, 86.37° and 78.42° relative to the loading direction, the first grain group appears to (i) have their slip orientations more close to the angle of 45° and (ii) have greater grain orientation differences among the three. Therefore, different stress-strain behaviour between grains during the monotonic tensile loading, Fig. 5(c), is mainly due to their different grain orientations, which influence the accumulated value of plastic slip.

5.2 Macroscopic cyclic stress–strain behaviour

The experimentally observed cyclic stress-strain behaviour, the 2nd cycle of the LCF fatigue loading, for the total strain ranges $\Delta \varepsilon_t$ of 2.4%, 2.0% and 1.6% are shown in Fig. 6. It can be seen in Fig. 6 that the experimentally observed stress–strain responses during the tension-compression loading cycle were in good agreement with the model predictions. This indicates that the CPFEM model can predict the macroscopic cyclic plasticity of GH4169 superalloy. Considering the heavy

computational cost, the LCF simulation of the cyclic behaviour of GH4169 superalloy was only performed up to 10 cycles of the LCF fatigue loading.

Fig. 7(a)-(c) shows the cyclic stress-strain loops of the specimen ($\Delta\varepsilon_t$=2.4%) at the 1st, 3rd and 10th fatigue cycles, respectively. As shown in Fig. 7(a), the model prediction is in good agreement with the experimental data for the 1st fatigue cycle. Such a good agreement between the model prediction and experimental observation can be also found for the 3rd fatigue cyclic loading, Fig. 7(b). However, a worse agreement between model prediction and experimentally observed stress–strain response can be seen in Fig. 7(c) for the 10th fatigue cycle. In this case, the model tends to predict a higher level of stresses for both the tension and compression phases. This can be related to the fact that the present model does not take into account the material's softening effect due to cyclic loading. We could have included more plasticity parameters, for example an internal state variable describing the softening effect, like adopted previously by Xu et al[37]. However this would make the model more complex than what is needed for the present work. Here the focus is to study whether the present model is capable to predict both the fatigue crack initiation behaviour and the fatigue life time. The model used in this paper saved computational time up to 35% due to its simplified form compared with the model used in preivous work[38]. Fig. 7(d)–(f) shows the cyclic stress-strain loops of the specimen ($\Delta\varepsilon_t$=1.6%) at the 1st, 3rd and 10th fatigue cycles, respectively. In general, a good agreement between the model prediction and the experimental data can be seen in Fig. 7(d) and (e). However, a worse agreement for both the tension and compression phases can also been observed in Fig. 7(f) for the 10th fatigue cycle. Since the degree of inconsistency in Fig. 7(f) for $\Delta\varepsilon_t$=1.6% (a less plasticity) is smaller than that for $\Delta\varepsilon_t$ =2.4% (a higher plasticity), Fig. 7(c), this confirms that the observed inconsistency between model prediction and experimental data is related to the simplified but more efficient approach adopted in our CPFEM model.

5.3 Prediction of fatigue crack initiation and fatigue life

Fig. 8 shows distributions of both the accumulated plastic slip and energy dissipation after 10th fatigue cycles for the specimen tested with the total strain amplitude of 2.0%. The presence of high levels of both the accumulated plastic slip and energy dissipation can be seen at the triple points and close to grain boundaries within one side of the grains. This indicates that the fatigue crack initiation is likely to occur at these stress/strain concentration areas. The model prediction in terms of the fatigue damage areas is consistent with the microstructural observation, Fig. 9, where the presence of persistent slip bands at grain interiors, at the triple points and close to grain boundaries are revealed. The presence of persistent slip bands in some specific grains can be related to their different orientations relative to adjacent grains. This location-dependent fatigue damage (i.e. both the accumulated plastic slip in Fig. 8(a) and the accumulated energy dissipation in Fig. 8(b)) seem to be consistent with the model prediction in terms of grain orientations between grain group 1 that consists of grains 1 to 3 and grain group 2 that consists of grains 4 to 6, as described in Fig. 5(c).

The fatigue life until failure of GH4169 LCF specimens were calculated based on Eqs. (12) and (13). The first step was to determine the critical accumulated plastic slip p_{crit} in Eq. (12) and the critical accumulated energy dissipation W_{crit} in Eq. (13) through fitting to experimental data. All plastic slip and energy dissipation were obtained from the same location of the RVE microstructure, i.e. at the triple point of grains as indicated by point A in Fig. 8. The model predicted accumulated plastic slip and energy dissipation at this triple point were then obtained up to 10 cycles of LCF fatigue. Fig. 10 shows that the accumulated plastic slip and energy dissipation exhibits a nearly linear relationship, cycle-by-cycle, with the increase in the number of fatigue cycles (up to 10 cycles). Therefore, it is reasonable to assume that both the plastic slip and energy dissipation in GH4169 superalloy accumulate with a constant rate during the LCF fatigue cycles.

Here a LCF specimen with the total strain amplitude of 1.6% was used to determine the critical value of p_{crit} and W_{crit}. Then the same critical values were

applied to each LCF specimens with the total strain amplitudes of 2.4%, 2.0%, 1.2%, 1.0% and 0.8%. It should be pointed that the critical value should be a fundamental quantity. Once determined, it should be possible to predict the occurrence of crack initiation over a range of strain amplitude [12, 27, 28]. All fatigue life data of specimen can be found in Ref.[39]. Fig. 11 shows the model predicted fatigue lives until failure along with a comparison to the experimental observed results of LCF tested specimens. It can be seen in Fig. 11 that almost all LCF life data can be predicted within a scatter band of factor 2. This indicates that both the accumulated plastic slip and energy dissipation as FIPs would be accurate enough for predicting LCF life of GH4169 superalloy. It is worthwhile noting that the slip-based and energy-based LCF damage criteria, Fig. 11, led to the same prediction results at the low strain amplitudes (i.e. higher LCF lives), whereas the energy-based LCF damage criteria provided a higher accuracy in terms of fatigue life prediction for LCF tests with the higher total strain amplitudes. In addition, at higher strain amplitude of 2.4%, it occurs a mismatch between prediction and experiment results. The overestimated fatigue life is mainly due to the plane-strain model which has also been proposed by Dunne et al.[12].

5.4 Stress distributions at meso-scale

The distributions of stresses and strains at the meso-scale along the loading direction (i.e. σ_{11} along x direction) are shown in Fig. 12(a) and (b) for the loaded state at the maximum strain of 1.0% and in Fig. 12(c) and (d) for the unloaded state after the specimen was tensile strained to 1.0%. In other words, the stresses and strains in Fig. 12(c) and (d) are residual stresses and strains, whereas those in Fig. 12(a) and (b) are the sum of applied and residual stresses and strains. In detail, grain 7 in Fig. 12(b) has a strain level smaller than the average at the loaded state but has a strain level larger than the average at the unloaded state among the three grains 7 to 9, Fig. 12(d). In terms of the stress, grain 7 in Fig. 12(a) has a stress level higher than the average at the loaded state but has a stress level smaller than average at the unloaded state of three grains 7 to 9, Fig. 12(c). Accordingly, grains 8 and 9 show the opposite

trend in Fig. 12(a)–(d). Such different local stress and strain behaviour in grains 7 to 9 are related to their different grain orientations relative to the loading direction. The slip system angles of these three grains, relative to the loading direction, were obtained from the model. Slip system of grain 7 has an angle of 81.29° to the loading direction. Similarly, grain 8 and grain 9 have angles of 46.07° and 65.08° to the loading direction. According to the model predicted results, the grain with its slip system orientated with an angle of approximate 45° to the loading direction tends to be softer and thus such grain tends to show a relatively lower stress level but a higher strain level. This observation is consistent with the classic Schmid's law[40]. Finally it is worthwhile to mention that these observed grain orientation dependency of the mechanical responses at the meso-scale are consistent with the previous studies[41,42].

5.5 Different sets of grain orientations

Three sets of grains with different grain orientations (cases 1 to 3) were employed into the present CPFEM model to study their effects on both the macroscopic and meso-scale material behaviour. This also helps to determine whether the present CPFEM model consisting of 150 grains would be representative of a texture-free polycrystalline material. Case 1 has been mainly used to study both the tensile and fatigue behaviours of GH4169 superalloy and is thus used here as a reference condition. As shown in Fig. 13, both case 2 and case 3 have a similar stress–strain behaviour from the model prediction. All three cases are in good agreement with the experimental data. This confirms that 150 grains used in our model can provide a typical macroscopic stress–strain behaviour representative of a polycrystalline material that usually consists of millions of grains. Furthermore, the scatter in predicting the fatigue crack initiation life (Fig. 11) between these three sets is relatively low that indicates the grain orientation has less influence on the macroscopic mechanical behaviour.

Fig. 14 shows the stress distribution contour plots at the maximum strain of 1.0% for the 10th fatigue cycles, for case 1, case 2 and case 3, respectively. As show in Fig.

14, three grain orientation cases show different stress and strain concentrations at the meso-scale. This reaffirms that different grain orientations among the selected grain groups would lead to the different stress distributions. In addition, some interesting phenomenon can be seen in Fig. 14(b). The three grains with their labels A, B and C in Fig. 14(b) have their slip system angles of 65.31°, 73.78° and 81.53° relative to the loading direction, respectively. Accordingly to the discussion made in section 5.2 about grain 9 with an angle of 65.08°, grain A and grain B that belong to the "soft" behaviour group would exhibit a lower local stress. However, Fig. 14 clearly shows an opposite trend. This different distribution of the local stress and strain concentration within grains is possibly due to the adjacent grain arrangements and their interaction[38]. In other words, the elastic and plastic responses of an individual grain contributes to the local stress and strain concentration at grain boundaries to satisfy both the stress equilibrium and strain compatibility. This also accounts for that the stress and strain concentration tends to be inclined to the grain boundaries areas. The different stress distributions shown in Fig. 14 also indicates that fatigue crack is more prone to initiate at grain boundary areas where the highest stress concentration is present.

6. Conclusions

A crystal plasticity finite element model has been employed to interpret the low cycle fatigue behaviour of GH4169 superalloy at both the macroscopic and meso-scale. The conclusions of this study are:

(1) Both the accumulated plastic slip and energy dissipation can be used as FIPs to determine the LCF fatigue cycles until failure. At higher strain amplitude, the energy dissipation tends to provide a better LCF fatigue life prediction. These have been compared to LCF experimental data and a good agreement is obtained.

(2) Fatigue damage is most likely to initiate at the triple points and grain boundaries where the presence of severe plastic slip and energy dissipation are observed. Grains with their active slip system orientated about 45° relative to the

loading direction tend to be softer, i.e. more plastic strain is accumulated in these grains. However, some grains will behave as "hard" grains even if their slip system angles are close to 45°.

(3) Different sets of grain orientations have a significant influence on the distribution of stresses between individual grains that determines different fatigue crack initiation locations. However, grain orientations have little influence on macroscopic stress-strain curve.

Acknowledgments

Reference

[1] J. Zrnik, M. Hazlinger, M. Zitnansky, Z.G. Wang, J. Mater. Sci. Technol. 11 (2009) 5-10.

[2] H. Zhang, Y.C. Wang, F. Liu, S.H. Ai, Q.S. Zang, Z.G. Wang, J. Mater. Sci. Technol. 18 (2002) 176-180.

[3] K.V.U. Praveen, V. Singh. Mater. Sci. Eng. A 485 (2008) 352-358.

[4] G. Chen, Y. Zhang, D.K. Xu, Y.C. Lin, X. Chen, Mater. Sci. Eng. A 655 (2016) 175-182.

[5] D.S. Wei, X.G. Yang, Int. J. Pressure Vessels Piping 86 (2009) 616-621.

[6] D. Peirce, R.J. Asaro, A. Needleman, Acta Metall. 30 (1982) 1087-1119.

[7] S.V. Harren, H.E. Dève, R.J. Asaro, Acta Metall. 36 (1988) 2435-2480.

[8] R. Becker, Acta Metall. 39 (1991) 1211-1230.

[9] C.J. Huang, D.Z. Li, C.R. Chen, Y.Y. Li, J. Mater. Sci. Technol. 17 (2001) 211-214.

[10] J.S. Wan , Z.F. Yue , X.L. Geng , Z.X. Lu, J. Mater. Sci. Technol. 18 (2002) 69-72.

[11] D.H. Zhang, S.Y. Li, J. Mater. Sci. Technol. 27 (2011) 175-182.

[12] F.P.E. Dunne, A. Manonukul, Proc. Roy. Soc. London A 460 (2004) 1881-1903.

[13] Y.J. Guan, B. Chen, J.W. Zou, T.B. Britton, J. Jiang, F.P.E. Dunne, Int. J. Plast. 88 (2016) 70-88.

[14] S. Keshavarz, S. Ghosh, Int. J. Solids Struct. 55 (2015) 17-31.

[15] S. Keshavarz, S. Ghosh, Acta Mater. 61 (2013) 6549-6561.

[16] S. Ghosh, G. S. Weber, Keshavarz, Mech. Res. Commun. 78 (2016) 34-46.

[17] F.P.E. Dunne, A.J. Wilkinson, R. Allen, Int. J. Plast. 23(2007) 273-295.

[18] A.M. Korsunsky, D. Dini, F.P.E. Dunne, M.J. Walsh, Int. J. Fatigue 29 (2007) 1990-1995.

[19] R.P. Skelton, Mater. Sci. Technol. 9 (1993) 1001-1008.

[20] R.P. Skelton, T. Vilhelmsen, G.A. Webster, Int. J. Fatigue 20 (1998) 641-649.

[21] Standard guide for electrolytic polishing of metallographic specimens, ASTM

2009.

[22] G.B. Thomas, R. Hales, J. Ramsdale, R.W. Suhr, G. Sumner, Fatigue Fract. Eng. Mater. Struct. 12 (2010) 135-153.

[23] G.M. Owolabi , H.A. Whitworth, J. Mater. Sci. Technol. 30 (2014) 203-212.

[24] Y.G. Huang, A User-material Subroutine Incorporating Single Crystal Plasticity in the Abaqus Finite Element Program, Harvard University, 1991.

[25] D. Peirce, R.J. Asaro, A. Needleman, Acta Metall. 31 (1983) 1951-1976.

[26] C.O. Frederick, P.J. Armstrong, Mater. High Temp. 24 (2007) 1-26.

[27] C.A. Sweeney, B. O'Brien, F.P.E. Dunne, P.E. Mchugh, S.B. Leen, Acta Mater 78 (2014) 341-353.

[28] D.F. Li, R.A. Barrett, P.E. O'Donoghue, N.P. O'Dowd, S.B. Leen, J. Mech. Phys. Solids 101 (2016) 44-62.

[29] A.B. Thakker, B.A. Cowles, Low strain, long life creep fatigue of AF2-1DA and INCO 718, 1983.

[30] H. Lim, J.D. Carroll, C.C. Battaile, B.L. Boyce, C.R. Weinberger, Int. J. Mech. Sci. 92 (2015) 98-108.

[31] K.S. Zhang, J.W. Ju, Z. Li, Y.L. Bai, W. Brocks, Mech. Mater. 85 (2015) 16-37.

[32] F. Sun, E.D. Meade, N.P. O'Dowd, J. Mech. Phys. Solids 113 (2018) 35-55.

[33] D. Peirce, C.F. Shih, A. Needleman, Comput. Struct. 18 (1984) 875-887.

[34] T.J. Ypma, Siam Rev. 37 (1995) 531-551.

[35] F. Barbe, L. Decker, D. Jeulin, G. Cailletaud, Int. J. Plast. 17 (2001) 513-536.

[36] X. Sun, K.S. Choi, W.N. Liu, M.A. Khaleel, Int. J. Plast. 25 (2009) 1888-1909.

[37] L. Xu, X. Nie, J. Fan, M. Tao, R. Ding, Int. J. Plast. 78 (2016) 44-63.

[38] B. Lin, L.G. Zhao, J. Tong, Eng. Fract. Mech. 78 (2011) 2174-2192.

[39] X.C. Zhang, H.C. Li, X. Zeng, S.T. Tu, C.C. Zhang, Q.Q. Wang, Mater. Sci. Eng. A 682 (2017) 12-22.

[40] F. R. N. Nabarro, Philos. Mag. 14 (1966) 861-866.

[41] J.W Lu, W. Sun, A. Becker, Int. J. Mech. Sci. 105 (2016) 315-329.

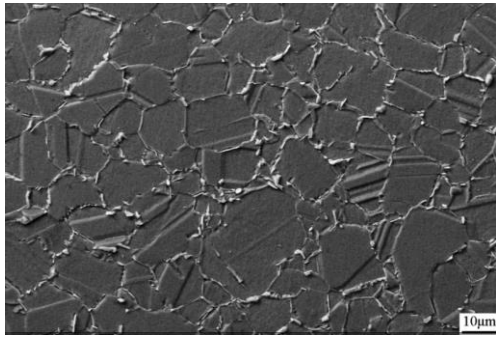[42] D.L. Mcdowell, F.P.E. Dunne, Int. J. Fatigue 32 (2010) 1521-1542.

Figure list:

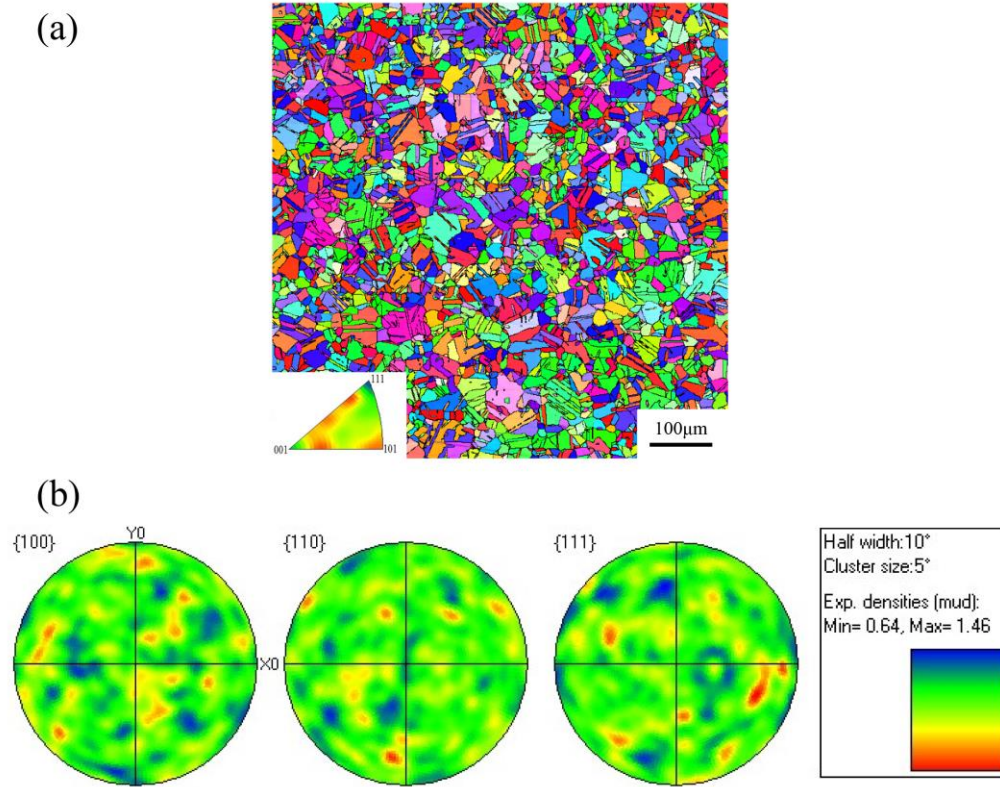**Fig. 1.** SEM micrograph of the GH4169 superalloy showing the equiaxed grain structure.

Fig. 2. (a) EBSD orientation map of GH4169 superalloy, (b) pole figures of the EBSD map showing a typical texture-free microstructure.
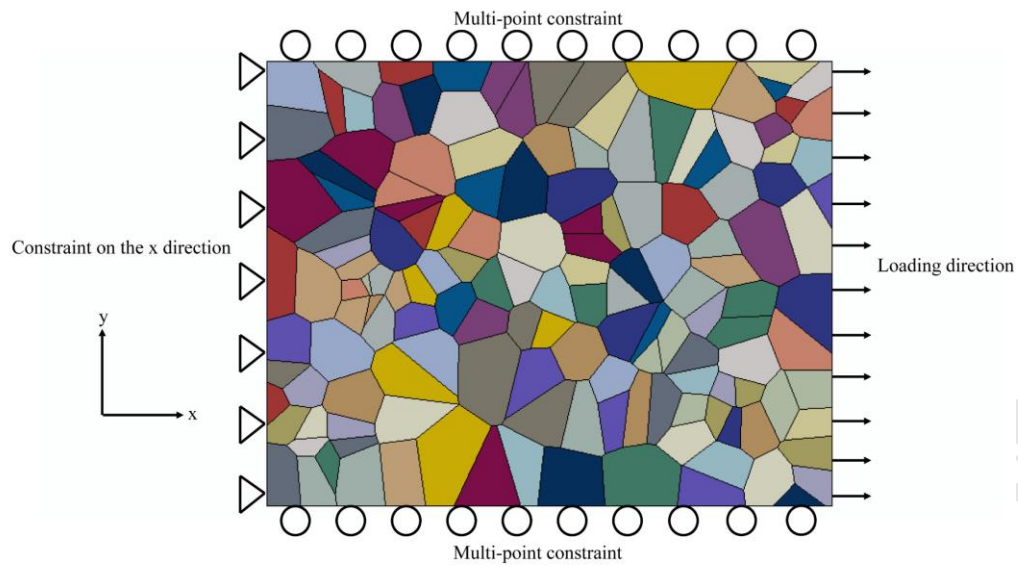
Fig. 3. RVE type microstructure established representative of the observed microstructure of GH4169 superalloy.
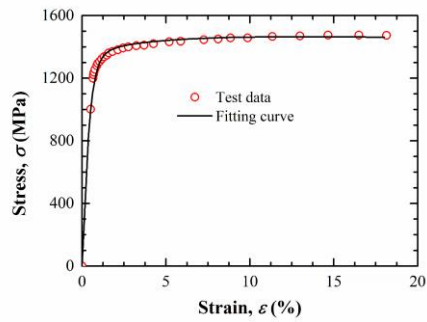

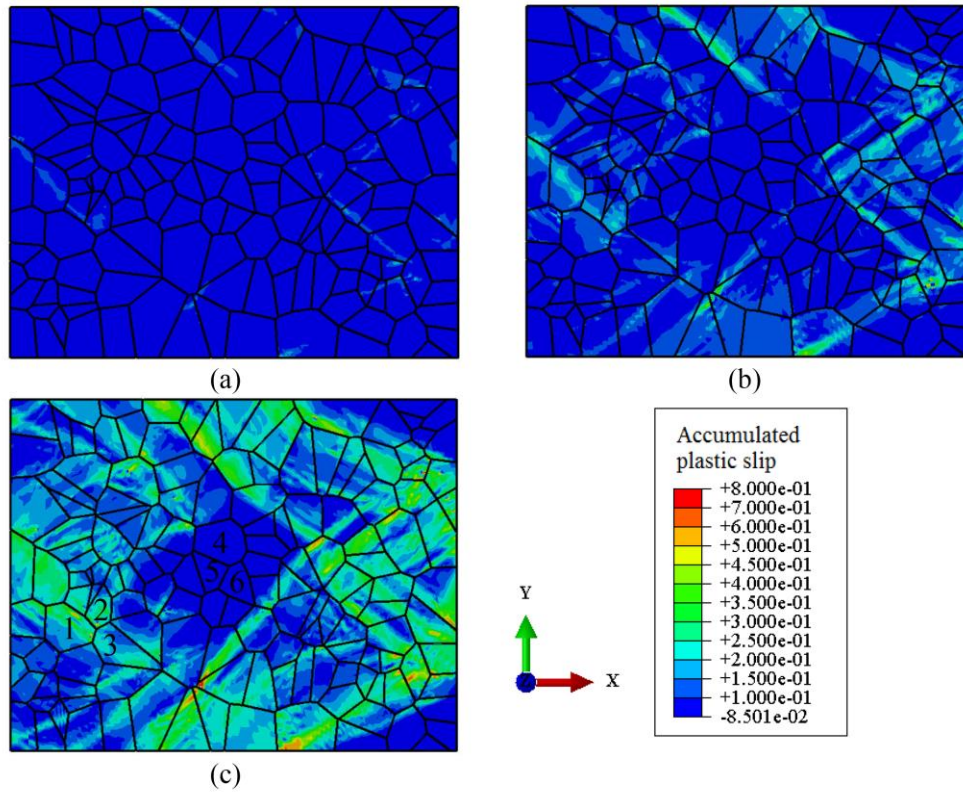**Fig. 4.** Comparison of CPFEM simulated macroscopic stress–strain curve with that obtained by uniaxial tensile testing.

Fig. 5. Model predicted plastic slip of GH4169 superalloy during the monotonic uniaxial tensile loading to enginering strains of (a) 3.5%, (b) 7% and (c) 13%.
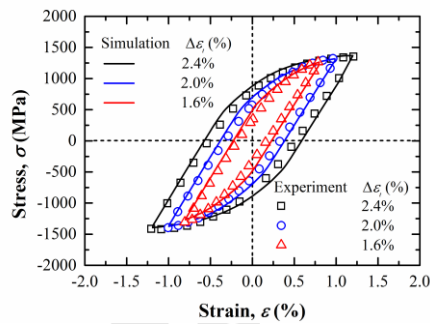
Fig. 6. CPFEM model predicted cyclic stress–strain responses of the 2nd fatigue cycle that are compared with the LCF experimntal data obtained at a range of total strain amplitudes.
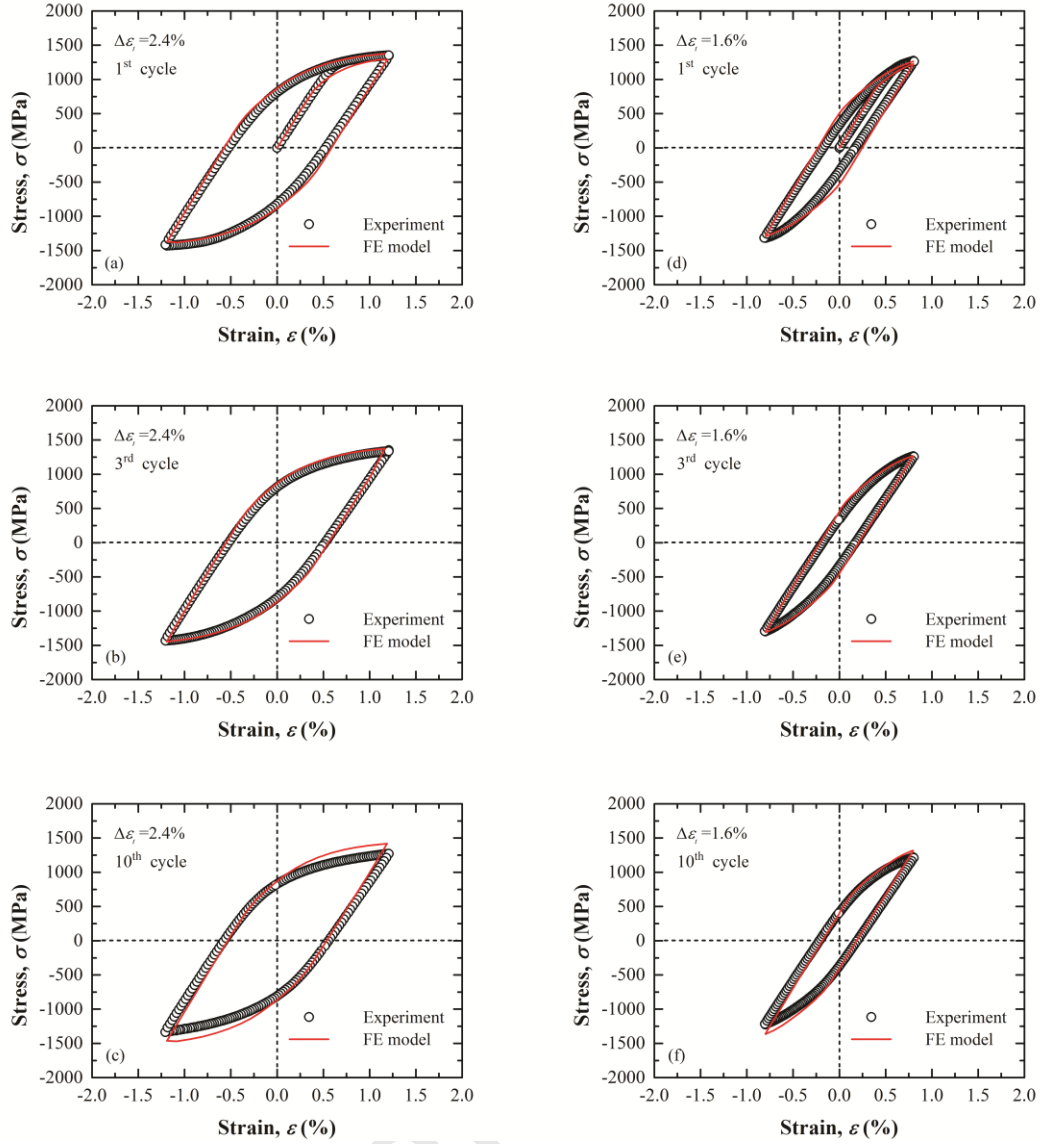
Fig. 7. Comparison of hysterisis loops between model predictions and experimental data for different fatigue loading cycles: (a) 1st cycle, $\Delta\varepsilon_t$=2.4%, (b) 3rd cycle, $\Delta\varepsilon_t$ =2.4%, (c) 10th cycle, $\Delta\varepsilon_t$ =2.4%, (d) 1st cycle, $\Delta\varepsilon_t$=1.6%, (e) 3rd cycle, $\Delta\varepsilon_t$ =1.6%, (f) 10th cycle, $\Delta\varepsilon_t$ =1.6%.
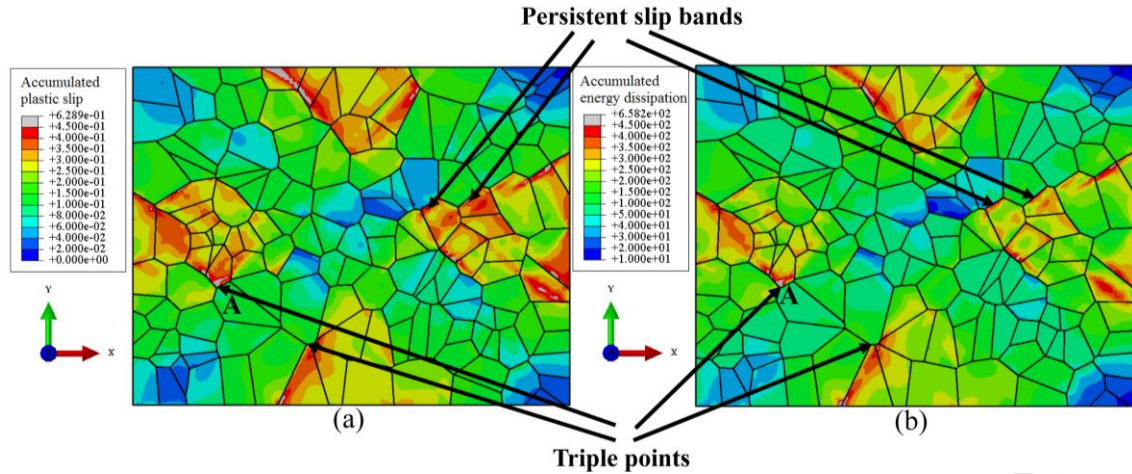
Fig. 8. Model predicted fatigue damage at the maximum tensile strain of 1.0% at the end of 10th fatigue cycle for the specimen tested with a total strain amplitude of 2.0%: (a) accumulated plastic slip, (b) accumulated energy dissipation. Note: Point A in each figure indicates the area ued for calulating critical fatigue damage indacator parameters.
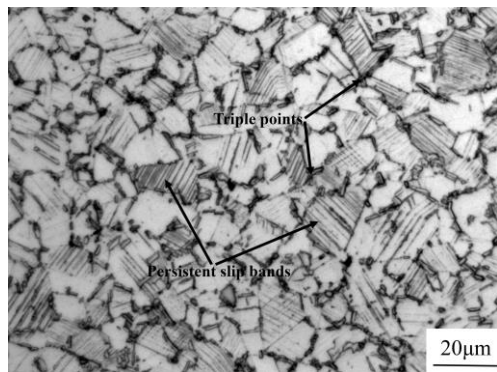

Fig. 9. Optical micrograph of a LCF fatigue tested specimen with a total strain amplitude of 2.0%. Note: The microstructure examination was made on a specimen that had been extracted from the location near to the fatigue fracture surface.
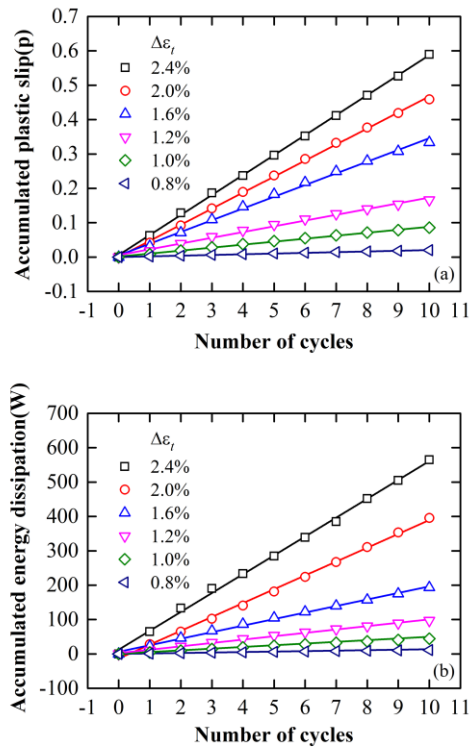
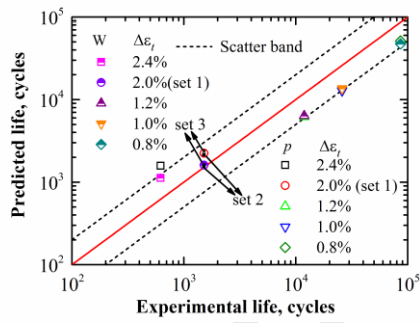**Fig. 10.** Nearly linear increase of (a) accumulated plastic slip, (b) accumulated energy dissipation.

Fig. 11. Life prediction with different FIPs: accumulated plastic slip and energy dissipation.
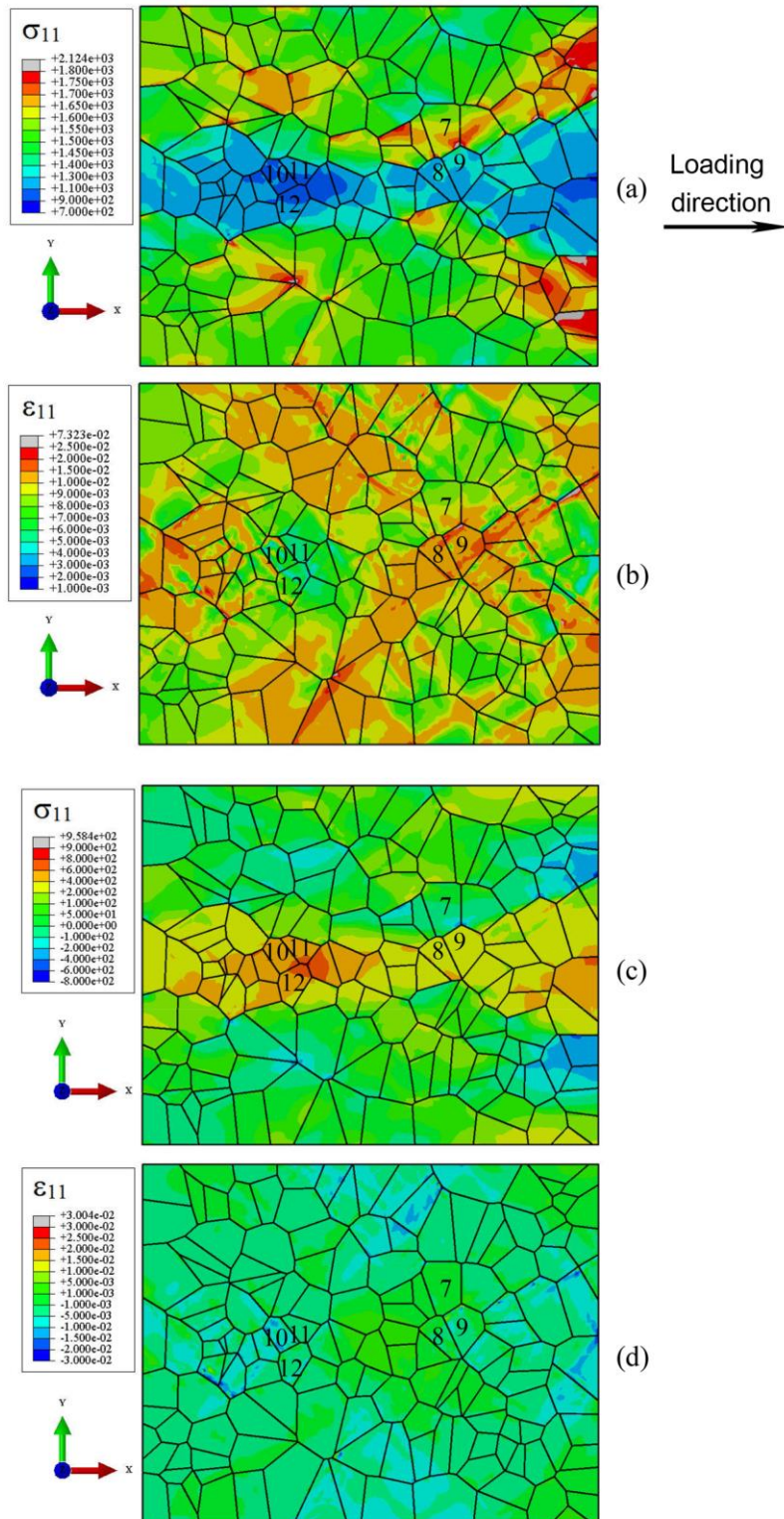
Fig. 12. Model predicted distrbution of the maximum principal stresses and strains at a LCF fatigue loaded specimen: (a) and (b) σ_{11} and ε_{11} at the loaded state to the maximum strain of 1.0%, (c) and (d) σ_{11} and ε_{11} at the unloaded state after the specimen was loaded to the maximum strain of 1.0%.
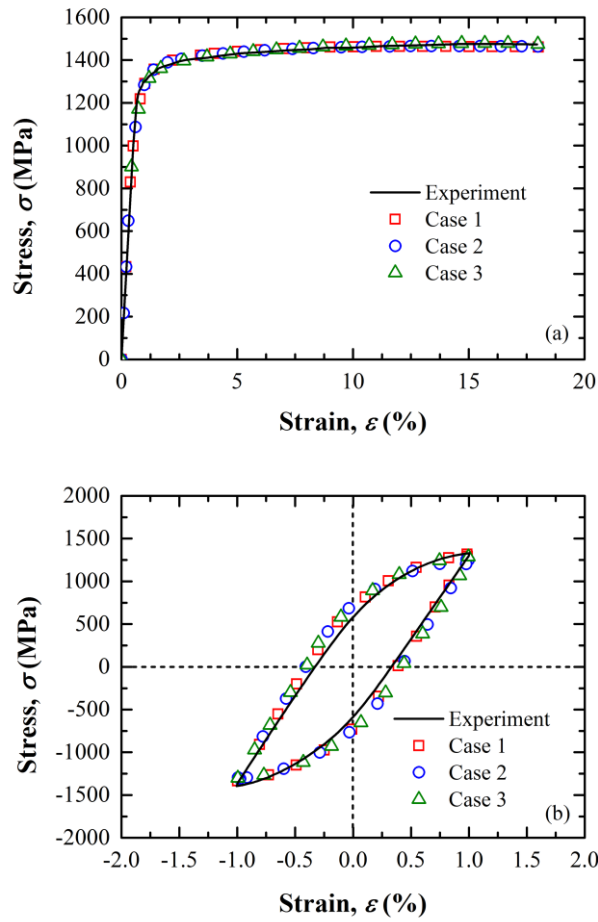
Fig. 13. A comparison of model predictions and experimental tensile and LCF fatigue stress-strain curves for different sets of grain orientations: (a) tensile loading, (b) LCF fatigue loading with the total strain amplitude of 2.0%.
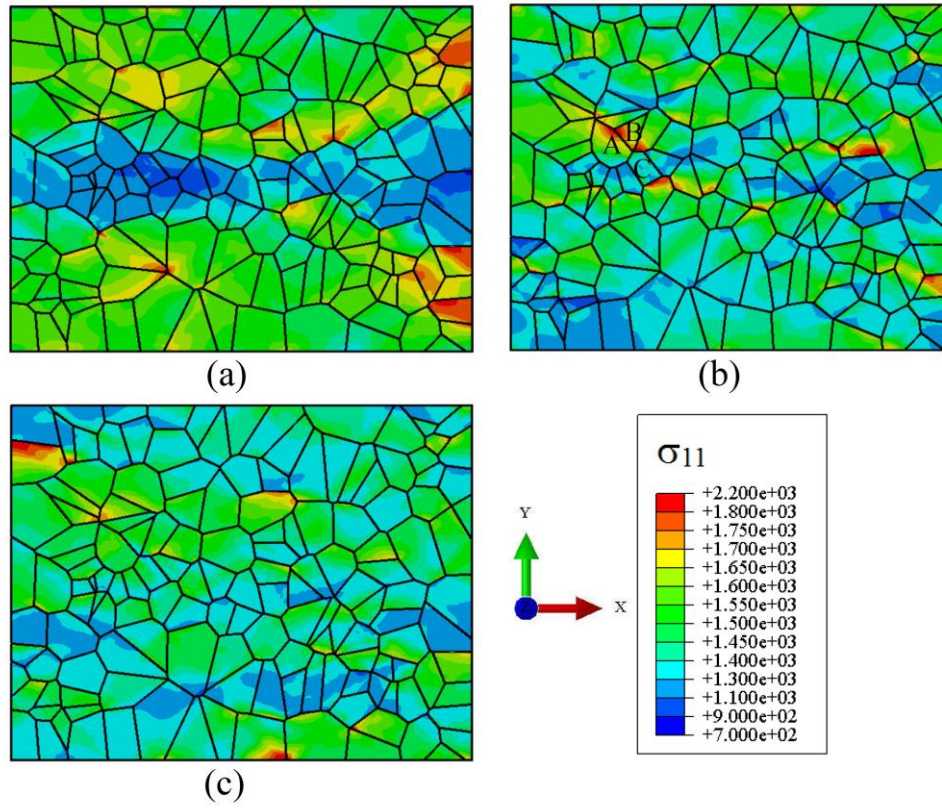
Fig. 14. Stress distribution with different sets of orientations at maximum strain load condition of strain amplitude 2.0%: (a) case 1, (b) case 2, (c) case 3.

Table list:

Table 1 Chemical composition of GH4169 superalloys (wt%).

C	Al	Si	Ti	Cr	Fe	Nb	Mb	Ni
0.82	0.44	0.18	1.16	19.55	18.93	5.19	2.74	Balance

Table 2 Constitutive parameters of GH4169 superalloys.

C_{11} (GPa)	C_{12} (GPa)	C_{44} (GPa)	n	$\dot{\gamma}_0$	h_0 (MPa)	g_∞ (MPa)	τ_0 (MPa)	C (MPa)	D
266	114	76	100	0.001	200	650	315	39500	475